The Astrophysical Journal, 933:149 (8pp), 2022 July 10 https://doi.org/10.3847/1538-4357/ac729c

Particle Acceleration in Relativistic Shearing Flows: Energy Spectrum

Frank M. Rieger[1,2] and Peter Duffy[3]
[1] Institute for Theoretical Physics, University of Heidelberg, Philosophenweg 16, D-69120 Heidelberg, Germany; f.rieger@uni-heidelberg.de
[2] Max-Planck-Institut für Kernphysik, Saupfercheckweg 1, D-69117 Heidelberg, Germany
[3] School of Physics, University College Dublin, Belfield, Dublin 4, Ireland
Received 2022 April 20; revised 2022 May 20; accepted 2022 May 22; published 2022 July 11

Abstract

We consider the acceleration of charged particles in relativistic shearing flows, with Lorentz factor up to $\Gamma_0 \sim 20$. We present numerical solutions to the particle transport equation and compare these with results from analytical calculations. We show that in the highly relativistic limit the particle energy spectrum that results from acceleration approaches a power law, $N(E) \propto E^{-\tilde{q}}$, with a universal value $\tilde{q} = (1 + \alpha)$ for the slope of this power law, where α parameterizes the power-law momentum dependence of the particle mean free path. At mildly relativistic flow speeds, the energy spectrum becomes softer and sensitive to the underlying flow profile. We explore different flow examples, including Gaussian and power-law-type velocity profiles, showing that the latter yield comparatively harder spectra, producing $\tilde{q} \simeq 2$ for $\Gamma_0 \simeq 3$ and Kolmogorov turbulence. We provide a comparison with a simplified leaky-box approach and derive an approximate relation for estimating the spectral index as a function of the maximum shear flow speed. These results are of relevance for jetted, high-energy astrophysical sources such as active galactic nuclei, since shear acceleration is a promising mechanism for the acceleration of charged particles to relativistic energies and is likely to contribute to the high-energy radiation observed.

Unified Astronomy Thesaurus concepts: High energy astrophysics (739); Non-thermal radiation sources (1119); Ultra-high-energy cosmic radiation (1733); Active galactic nuclei (16); Relativistic jets (1390)

1. Introduction

The relativistic outflows from gamma-ray bursts and active galactic nuclei (AGNs) are generically expected to exhibit velocity shearing across the flow. In AGNs, for example, lateral shearing could be intrinsically (jet−wind topology) or extrinsically (interaction with the environment, matter entrainment) induced. The growing realization that such shear flows can be conducive to efficient Fermi-type particle acceleration (e.g., Lemoine 2019; Rieger 2019) has in recent times motivated a variety of studies exploring its role for the production of high-energy particles and emission (e.g., Webb et al. 2018, 2019, 2020; Rieger 2019; Rieger & Duffy 2019, 2021; Merten et al. 2021; Tavecchio 2021; Wang et al. 2021). Early models of particle transport in shearing flows implied that in the absence of radiative losses the accelerated particle (momentum) distribution in steady state follows a power-law spectrum, $f(p) \propto p^{-s}$, with spectral index $s = (3 + \alpha)$ for a mean scattering time scaling as $\tau \propto p^{\alpha}$ (Berezhko & Krymskii 1981; Berezhko 1982; Rieger & Duffy 2006). It was subsequently shown, however, that this index only applies to the highly relativistic ($\beta \to 1$) limit (Webb et al. 2018, 2019; Rieger & Duffy 2019). In particular, subrelativistic flow speeds lead to much softer spectra. The reason for this is that in diffusive shear acceleration the momentum gain, for a particle scattered across the flow, competes with diffusive escape from the system (Jokipii & Morfill 1990; Rieger & Duffy 2006), thereby affecting the particle spectrum.

The leaky-box model for the spatially averaged, steady-state momentum phase-space distribution $f(p)$ captures these essential features (Rieger & Duffy 2019). With a momentum diffusion coefficient D_p, escape timescale $\tau_{\rm esc}$ and injection $Q(p)$, this equation is

$$\frac{1}{p^2}\frac{\partial}{\partial p}\left(p^2 D_p \frac{\partial f}{\partial p}\right) - \frac{f}{\tau_{\rm esc}} + Q(p) = 0, \tag{1}$$

in the regime where radiative losses are negligible. With a momentum-dependent mean free path, $\lambda \propto p^{\alpha}$, the diffusion coefficient $D_p \propto p^{2+\alpha}$ leads to an acceleration timescale that decreases with momentum $t_{\rm acc}(p) = p^2/([4 + \alpha]D_p) \propto p^{-\alpha}$ as higher-momentum particles are scattered across a greater part of the shear flow. The same scattering gives rise to a spatial diffusion coefficient $\kappa(p) \propto \lambda \propto p^{\alpha}$ and an escape timescale $\tau_{\rm esc} = (\Delta r)^2/2\kappa(p) \propto p^{-\alpha}$, where Δr is the width of the shear region. That the acceleration and escape timescales have the same momentum dependence is a key requirement of any Fermi-type acceleration process to result in a power-law distribution. With $f \propto p^{-s}$ inserted into Equation (1), the index is

$$s = \frac{(3 + \alpha)}{2} + \sqrt{\frac{(3 + \alpha)^2}{4} + (4 + \alpha)\frac{t_{\rm acc}}{\tau_{\rm esc}}}, \tag{2}$$

recovering the limit of $s = 3 + \alpha$ when $t_{\rm acc} \ll \tau_{\rm esc}$.

The full transport equation for the phase-space density $f(r, p)$ includes both momentum and spatial diffusion terms with a spatially dependent flow velocity $c\beta(r)$. In principle, this will change the prediction for the spectral index in the leaky-box limit of Equation (2). The aim of this paper is to calculate spectral indices for the full transport equation and to examine how the details of the flow profile affect the value for s. To achieve this, we compare in the following (Section 2) numerical solutions of the relativistic particle transport equation for three major key flow profiles, and we discuss them in the context of this simplified leaky-box approach in Section 3. The results provide a foundation for connecting

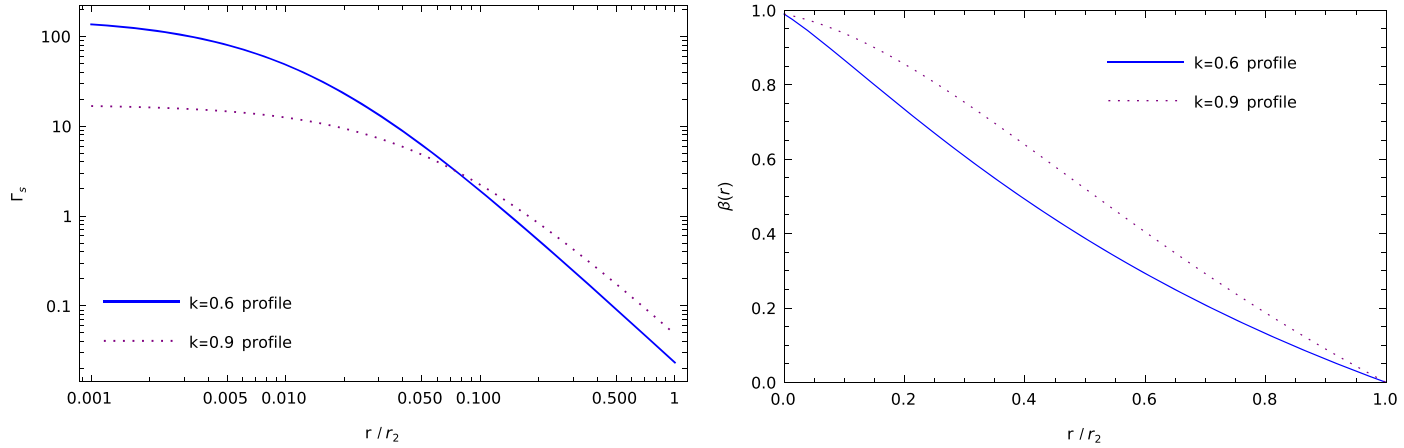

Figure 1. Left: evolution of the shear coefficient Γ_s, Equation (4), as a function of the normalized radial coordinate r/r_2 for the velocity profiles explored in Figure 2; see Equation (6) and plot to the right, with $\beta_0 = 0.99$. The solid line corresponds to the profile with $k_3 = 0.6$, while the dotted curve corresponds to the one with $k_3 = 0.9$. In both cases, Γ_s takes on large values but remains bounded as $r \to 0$, while approximately showing a $\propto r^{-2}$-dependence on larger scales. Right: corresponding velocity profiles as a function of the normalized radial coordinate r/r_2, with line style identification as to the left (solid: $k_3 = 0.6$; dotted: $k_3 = 0.9$).

momentum power-law spectral indices to specific flow velocity profiles.

2. Particle Transport in Relativistic Flows

The phase-space evolution of energetic charged particles in relativistic flows obeys a diffusive particle transport equation (e.g., Webb 1989). In the case of a relativistic jet with cylindrical shear flow $\beta(r) = u_z(r)/c$, the corresponding, steady-state particle transport equation for the phase-space distribution function $f(r, p)$ with source term Q takes the form (Webb et al. 2018)

$$\frac{1}{p^2}\frac{\partial}{\partial p}\left(p^4\Gamma_s\tau\frac{\partial f}{\partial p}\right) + \frac{1}{r}\frac{\partial}{\partial r}\left(\kappa r\frac{\partial f}{\partial r}\right) + Q = 0, \tag{3}$$

where $\tau = \lambda/c$ is the mean scattering time, $\kappa = c^2\tau/3$ is the spatial diffusion coefficient, and

$$\Gamma_s \equiv \Gamma_s(r) = \frac{c^2}{15}\,\gamma_b(r)^4\left(\frac{d\beta}{dr}\right)^2 \tag{4}$$

denotes the relativistic shear flow coefficient, with $\gamma_b(r)^2 = 1/(1-\beta(r)^2)$ (Rieger & Duffy 2006; Webb et al. 2018). Formally, Equation (3) is a mixed-frame particle transport equation where the momentum variable p is evaluated in the comoving flow frame, while the spatial coordinate r is measured in the laboratory frame. This utilizes the fact that the scattering process is most conveniently evaluated in the local fluid frame. In general, the scattering time τ can be a function of space and momentum. In this paper we focus on the r-independent case $\tau \equiv \tau(p) = \tau_0 p^{\alpha}$, $\alpha > 0$. With this choice, Equation (3) becomes a separable, elliptical partial differential equation. In quasi-linear theory α is related to the particle mean free path $\lambda = c\tau \propto p^{2-q}$, where $\alpha = 2 - q$ and q is the power spectrum of the turbulence with $q = 1$ for Bohm, $q = 3/2$ for Kraichnan, and $q = 5/3$ for Kolmogorov (Liu et al. 2017).

2.1. A Comparison with Analytical Results by Webb et al. (2018)

By solving the particle transport equation, the dependence of $f(r, p)$ on the flow speed β can be explored. In particular, Webb et al. (2018) have presented results of Equation (3) for the special case where $\tau(r, p) \propto p^{\alpha}/[\gamma(r)^2 r(d\beta/dr)]$, chosen so as to yield analytical solutions. Requiring the scattering time τ to be nonsingular throughout most of the jet, this constraint can be related to some specific flow velocity profiles. For their model ansatz Equation (36), for example, the resultant τ is weakly dependent on r, $\tau \propto (1 + \epsilon/r)$, where $\epsilon/r \ll 1$, but has the property $\tau \to \infty$ as $r \to 0$. Since this property is restricted to a small region near the jet axis ($r = 0$), this does not necessarily have to lead to unphysical results. However, since Γ_s is very large in this region, a straightforward comparison with observations may not be possible. With boundary conditions $\partial f/\partial r \to 0$ as $r \to 0$ and $f(r_2, p) = 0$ at the outer jet boundary r_2, Webb et al. (2018) showed that the particle energy distribution at high energies approaches a power-law particle distribution $f(r, p) \propto p^{-s}$, with index s given by

$$s = \frac{3+\alpha}{2} + \sqrt{\frac{(3+\alpha)^2}{4} + 5\pi^2\left[\ln\left(\frac{1+\beta_{02}}{1-\beta_{02}}\right)\right]^{-2}}, \tag{5}$$

where $\beta_{02} = (\beta_0 - \beta_2)/(1 - \beta_0\beta_2)$ is the relativistic relative velocity of the central jet velocity, β_0, to the outer velocity of the jet, $\beta_2 = \beta(r_2)$. Obviously, as β_0 becomes nonrelativistic, s increases significantly, implying very soft spectra. To explore consequences related to the singular τ-description, we employ a velocity profile following Webb et al. (2018),

$$\beta(r) = \frac{(1+\beta_0)/(1-\beta_0) - [(1 + r/\epsilon)]^{2k_3}}{(1+\beta_0)/(1-\beta_0) + [(1 + r/\epsilon)]^{2k_3}}, \tag{6}$$

but assume τ to be r-independent, i.e., $\tau \equiv \tau(p) = \tau_0 p^{\alpha}$. Here and in the following we choose a Kolmogorov-type turbulence ($q = 5/3$, i.e., $\alpha = 1/3$). The flow profile of Equation (6) takes on a maximum value β_0 at $r = 0$; $\epsilon \ll r_2$ is constrained by the requirement that $\beta(r_2) = 0$ (see Figure 1). Figure 2 shows examples of the evolution of the momentum spectral index s

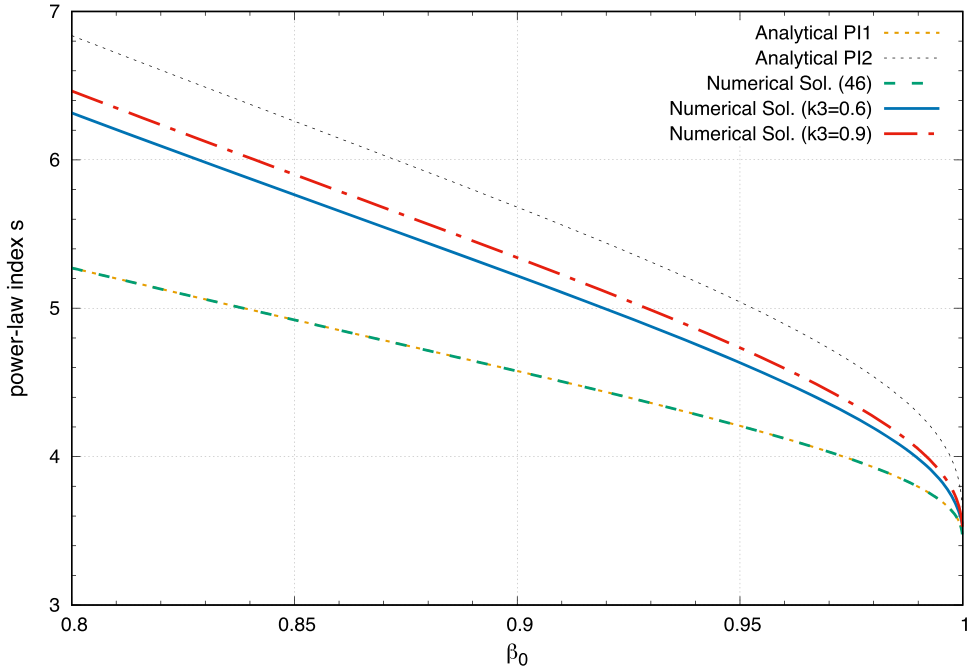

Figure 2. Evolution of the momentum power-law index s, where $f \propto p^{-s}$, as a function of the flow speed on the jet axis, $\beta_0 \equiv \beta(r=0)$, for a particle mean free path $\lambda = c\tau \propto p^{\alpha}$ with $\alpha = 1/3$ (corresponding to Kolmogorov-type turbulence $q = 5/3$). The dotted orange line (PI1) denotes the asymptotic spectral index as given in Equation (5) (see also Webb et al. 2018), and the dashed green line (on top) denotes the power-law index based on a numerical solution of the corresponding particle transport equation (Webb et al. 2018, Equation (46)). Both agree, and they characterize the momentum spectrum in the case where τ shows a weak r-dependence throughout most of the jet but has $\tau \to \infty$ as $r \to 0$. The solid blue line denotes the numerical solution for a velocity profile with $k_3 = 0.6$ in Equation (6), while the dashed–dotted red line denotes the one for $k_3 = 0.9$. For both cases an r-independent τ has been assumed. The dotted black line at the top gives the analytical asymptotic index as derived in Webb et al. (2019) for an r-independent τ but a different, nonsimilar flow profile (see main text below). For all cases, monoenergetic injection has been considered, and $\beta_2 = 0$ has been assumed at the outer jet boundary.

above injection as a function of jet flow speed on the axis, β_0, based on a numerical solution of Equation (3) with a finite element method using the default Pardiso direct solver (Wolfram 2022).

While all spectra approach the limiting value $s \to (3+\alpha)$ for ultrarelativistic speeds $\beta_0 \to 1$, there is a general trend for the momentum spectra to be softer than those based on a τ-description that becomes singular as $r \to 0$. While the power-law index in Equation (5) is seemingly independent of the velocity shape, through the value of k_3, this no longer applies to the r-independent case. This seems partly due to the fact that the average rate of momentum change for a particle, $\langle \Delta p/\Delta t \rangle$, is proportional to $\Gamma_s p\tau$ (Rieger & Duffy 2006; Liu et al. 2017). Since, for relativistic β_0, Γ_s takes on large values on small scales (see Figure 1), this is expected to dominate particle energization, in particular for the considered singular τ-description, thus leading to an apparent universal index evolution. We thus consider s, as defined in Equation (5), as giving a lower limit for velocity profiles of the type given by Equation (6).

2.2. A Comparison of Different Flow Profiles for Spatially Constant τ

For a spatially constant τ, on the other hand, Webb et al. (2019) have identified a class of concave-type velocity profiles,

$$\beta(r) = \tanh\left[\xi_0 - (\xi_0 - \xi_2)\left(\frac{r}{r_2}\right)^k\right], \quad k \geqslant 1, \tag{7}$$

with $\xi_0 = \mathrm{arctanh}(\beta_0)$ and $\xi_2 = \mathrm{arctanh}(\beta_2)$, that give analytical solutions of the particle transport Equation (3). Independently of the value of k (i.e., encompassing a variety of different shapes), they find an asymptotic power-law index for this case given by

$$s = \frac{3+\alpha}{2} + \sqrt{\frac{(3+\alpha)^2}{4} + 20 j_{0,1}^2 \left[\ln\left(\frac{1+\beta_{02}}{1-\beta_{02}}\right)\right]^{-2}}, \tag{8}$$

where $j_{0,1} \simeq 2.4048$ denotes the first zero of the $J_0(z)$ Bessel function of the first kind (Abramowitz & Stegun 1972). We find very good agreement between a numerical solution of Equation (3) for the particular case of $k = 2$ and this analytically derived expression. The power-law index, Equation (8), is comparable to, but softer than, the one in the previously considered case (where $\tau \to \infty$ as $r \to 0$), Equation (5), and may suggest that for spatially constant diffusion softer spectra are obtained. To investigate this in more detail, we numerically solve the particle transport equation, Equation (3), for three different velocity class profiles: the linear case

$$\beta_l(r) = \beta_0(1 - (r/r_2)); \tag{9}$$

a Gaussian profile, with $a_g > 0$,

$$\beta_g(r) = \beta_0 \exp\left(-a_g\,[r/r_2]^2\right); \tag{10}$$

and a power-law dependence, with $b \geqslant 1$,

$$\beta_p(r) = \frac{\beta_0}{(1 + a_p^2\,[r/r_2]^2)^{b/2}}. \tag{11}$$

The Gaussian and power-law profiles are convex over most of the interval and in that respect different from the concave

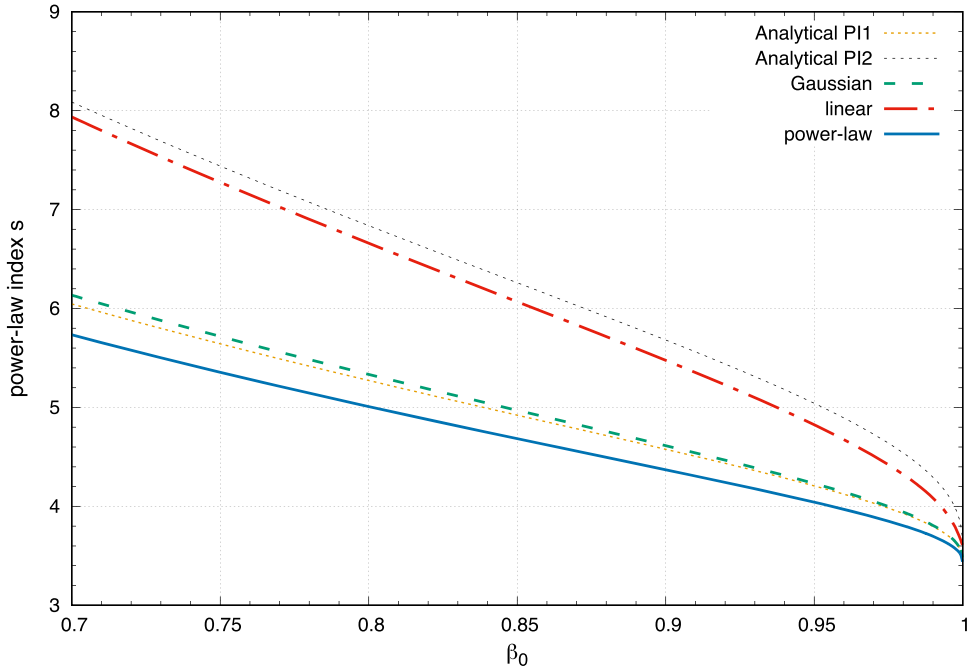

Figure 3. Evolution of the momentum power-law index s, where $f \propto p^{-s}$, as a function of the flow speed on the jet axis, $\beta_0 \equiv \beta(r=0)$, for spatially constant $\tau \propto p^{\alpha}$ with $\alpha = 1/3$. The dotted blue line (PI1) denotes the asymptotic spectral index as given in Equation (5) (Webb et al. 2018), and the upper, dotted black line (PI2) denotes the asymptotic index as given in Equation (8) (Webb et al. 2019), both considering $\beta_2 = 0$. The dashed–dotted red line denotes the numerical solution for a linearly decreasing velocity profile, Equation (9), and the dashed green line denotes the one for a Gaussian velocity profile, Equation (10), with $a_g = 5$. While the index for a linear decreasing velocity profile is relatively soft and close to the one for a concave profile, Equation (7), the one for a Gaussian velocity profile is relatively hard and close to the singular τ case. Even harder momentum spectra are obtained, however, for a power-law-type velocity profile, Equation (11), with $a_p = 5$, $b = 2$ (solid purple line).

profile of Equation (7). For flow profiles of the type given by Equation (6), Γ_s is a monotonically decreasing function, with maximum values on the axis, while for flow profiles of the type given by Equation (7), Γ_s is a monotonically increasing function (for $k > 1$) that takes on a maximum value at the outer boundary. On the other hand, the linearly decreasing profile, Equation (9), results in a monotonically decreasing Γ_s, while profiles of the type given by Equations (10)–(11) result in a Γ_s that initially rises and peaks close to, but not on, the axis and then subsequently decreases monotonically (see Figure 7 in the Appendix). The numerical results for a monoenergetic source term with $p = p_0$ at $r = 0.1\, r_2$ are shown in Figure 3. As before, boundary conditions $\partial f/\partial r \to 0$ as $r \to 0$ and $f(r_2, p) = 0$ at the outer jet boundary r_2 have been applied. At high energies the particle distribution $f(r, p)$, evaluated at $r = 0.8\, r_2$, follows a power law with somewhat different index evolution. For the linearly decreasing velocity profile the spectra are relatively soft, with power-law index s close to the one for the concave profile of Equation (7) and to the one for a $k_3 = 0.9$ profile, Equation (6) (see Figure 2), while the spectra for a Gaussian velocity profile are relatively hard, with index very close to the one for the singular τ case, Equation (5). The hardest spectrum (e.g., at $\beta_0 = 0.95$ by $\Delta s \sim 0.2$ when compared to the singular one) is obtained for a power-law-type velocity profile, Equation (11). The latter result provides evidence that even for spatially constant diffusion, momentum spectra harder than the asymptotic index, Equation (5), can be obtained. At ultrarelativistic speeds, we observe $s \to (3 + \alpha)$ for all profiles.

2.3. Solutions for a Power-law-type Velocity Profile

As the power-law velocity profile yields the hardest spectra, we further explore two more cases, varying a_p and/or b in Equation (11). We consider, as before, monoenergetic injection with $p = p_0$ at $r = 0.1\, r_0$, and $\alpha = 1/3$. Figure 4 (left) shows a three-dimensional plot of $\log f(r, p)$ for the previous case $a_p = 5$, $b = 2$ over the spatial range $r = (0 - 1) r_s$ and a momentum range p above injection. Figure 4 (right) shows the r-dependence of the respective $f(r, p)$ for the three different power-law-type profiles at fixed momentum p, with the distribution functions appearing comparatively similar and satisfying the imposed boundary conditions. The dependence of s on β_0 is shown in Figure 5, which becomes harder for steeper profiles, i.e., for $a_p = \sqrt{50}$, $b = 2$ (red line) and $a_p = 5$, $b = 3$ (purple line). The indices for the latter cases appear close to each other, as their velocity shapes and shear coefficients appear relatively similar. In particular, power-law momentum indices $s \simeq 4$, corresponding to $N(E) \propto E^{-2}$, are achievable for flow Lorentz factors $\Gamma_0 \simeq 3$ ($\beta_0 \simeq 0.94$).

3. Comparison with the Leaky-box Spectrum

The above results illustrate that in general the power-law momentum index s depends on the shape of the bulk flow profile. In principle, this is to be expected, as particle energization satisfies $\langle \Delta p/\Delta t \rangle \propto \Gamma_s p \tau$. In this section we explore the extent to which these results can be recaptured by means of the simplified leaky-box Equation (1), where D_p is the momentum-space shear diffusion coefficient (Rieger & Duffy 2006) $D_p = \Gamma_s p^2 \tau =: D_0 p^{2+\alpha}$, with $\tau = \lambda/c \propto p^{\alpha}$ the (momentum-dependent) mean scattering time and Γ_s the shear coefficient as defined in Equation (4). The leaky-box approach assumes that all spatial dependencies, for example, the second term in Equation (3), can be approximated by some suitably chosen average escape term. Following Equation (1), the characteristic (comoving) shear particle acceleration timescale

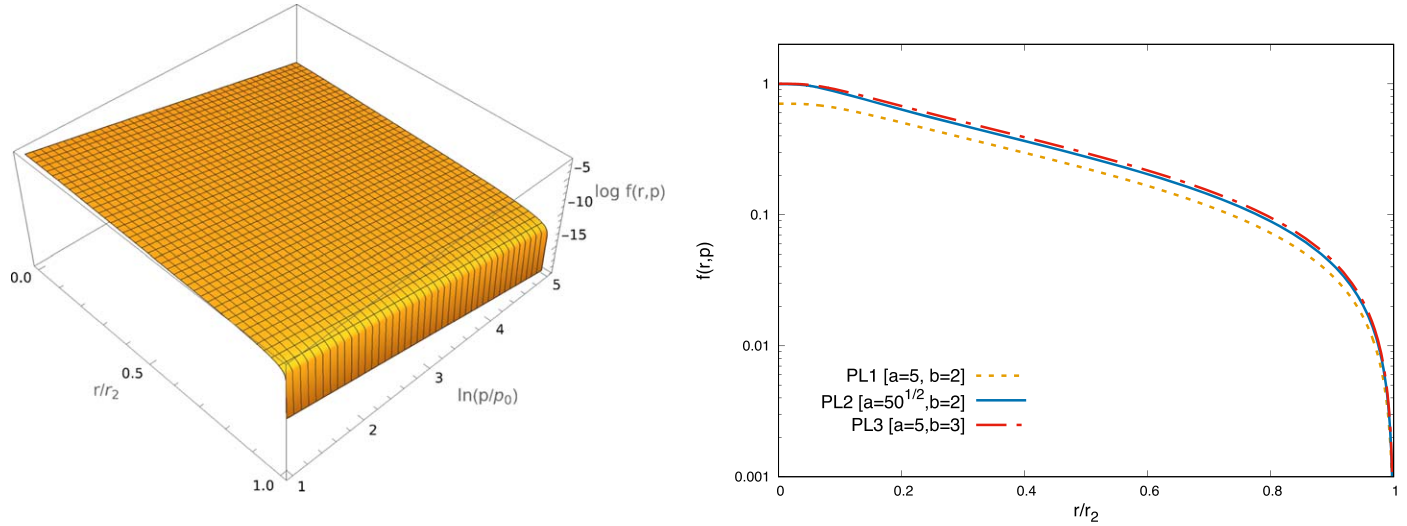

Figure 4. Left: three-dimensional plot of $f(r, p)$ for a power-law-type velocity profile, Equation (11), with $a_p = 5$, $b = 2$ and a flow speed on the axis of $\beta_0 = 0.95$. Right: exemplary illustration of the r-dependence of $f(r, p)$ at fixed $p = e^3\, p_0$ for power-law velocity profiles, Equation (11), with $a_p = 5$, $b = 2$ (dotted orange line), $a_p = \sqrt{50}$, $b = 2$ (solid blue line), and $a = 5$, $b = 3$ (dashed–dotted red line), all particle distribution functions being normalized to the value of f at $r = 0$ for the third profile. A flow speed on the axis of $\beta_0 = 0.90$ has been employed.

might be expressed as (e.g., Rieger 2019)

$$t_{\rm acc}(p) = \frac{c}{(4+\alpha)\Gamma_s\,\lambda} \propto p^{-\alpha}. \tag{12}$$

The escape time, on the other hand, is determined by cross-field transport and the width of the jet

$$\tau_{\rm esc}(p) = \frac{(\Delta r)^2}{2\,\kappa(p)} \propto p^{-\alpha}, \tag{13}$$

where $\kappa = \lambda c/3$ denotes the spatial diffusion coefficient and $\Delta r = (r_2 - r_0)$ (Rieger & Duffy 2019), where we take $r_0 = 0$.

The Green's function solution of Equation (1) for mono-energetic injection $Q_\delta(p) = Q_0\,\delta(p - p_0)$ is given by (see Rieger & Duffy 2019; Webb et al. 2020)

$$f(p) = f_0\, p^{-s_1}\, H(p_0 - p) + f_0\, p^{-s_2}\, H(p - p_0), \tag{14}$$

where the corresponding power-law indices are given by

$$\begin{aligned} s_{1,2} &= \frac{(3+\alpha)}{2} \mp \sqrt{\frac{(3+\alpha)^2}{4} + (4+\alpha)\frac{t_{\rm acc}}{\tau_{\rm esc}}} \\ &= \frac{(3+\alpha)}{2} \mp \sqrt{\frac{(3+\alpha)^2}{4} + \frac{2\,c^2}{3\,\Gamma_s r_2^2}}. \end{aligned} \tag{15}$$

For $t_{\rm acc} \ll \tau_{\rm esc}$, i.e., for relativistic shear flows, $s_1 \to 0$ and $s_2 \to (3+\alpha) = 10/3$ for $\alpha = 1/3$. For subrelativistic flows, on the other hand, the second term inside the square root becomes large, resulting in steep (soft) high-energy spectra.

However, even for an r-independent scattering time τ, the power-law expression in Equation (15) formally includes an explicit r-dependence (via Γ_s in $t_{\rm acc}$; see Equations (12) and (4)). In Rieger & Duffy (2019) we explored a possible way of treating this r-dependence, approximating $\gamma_b(r)^4 (d\beta/dr)^2$ in Γ_s, Equation (4), by $\langle \gamma_b(r)^2\, (d\beta/dr)\rangle^2$, where $\langle\rangle$ denotes averaging over r from 0 to r_2. Since for $\beta(0) = \beta_0$ and $\beta(r_2) = \beta_2$, $\langle \gamma_b(r)^2 (d\beta/dr)\rangle = -(1/[2\,r_2])\ln([1+\beta_{02}]/[1-\beta_{02}])$, where $\beta_{02} = (\beta_0 - \beta_2)/(1 - \beta_0\beta_2)$, this approximation then yields

$$s = \frac{(3+\alpha)}{2} + \sqrt{\frac{(3+\alpha)^2}{4} + 40\left[\ln\frac{(1+\beta_{02})}{(1-\beta_{02})}\right]^{-2}}, \tag{16}$$

for the particle distribution above injection (i.e., for $p > p_0$) in the leaky-box approach. This expression turns out to be close to the analytical result of Equation (5), reproducing well the qualitative behavior of s as a function of the on-axis flow speed β_0 (see also Webb et al. 2020). One obvious drawback of this approximation is, however, that it does not allow one to distinguish between different velocity shapes since the resultant expression is only a function of the on-axis β_0 and the outer β_2.

To improve on this in view of our current results, we use the original particle transport Equation (3) with a local, mono-energetic source term, applying separation of variables, $f(r,\ p) = h(r)\cdot g(p)$. Away from injection and assuming an r-independent τ, one then obtains the two differential equations,

$$\begin{aligned} \frac{1}{\Gamma_s}\frac{1}{r}\frac{\partial}{\partial r}\left(r\frac{\partial h(r)}{\partial r}\right) &= -\lambda^2\cdot h(r), \\ \frac{1}{\kappa\, p^2}\frac{\partial}{\partial p}\left(p^4\tau\frac{\partial g(p)}{\partial p}\right) &= \lambda^2\cdot g(p), \end{aligned} \tag{17}$$

where λ^2 is a constant to be determined by the boundary conditions. Replacing Γ_s by a suitable, spatially averaged $\langle\Gamma_s\rangle =: \tilde{\Gamma}_s/r_2^2$, then the first differential equation can be solved and has the general solution

$$h(r) = c_1 J_0\left(\lambda\sqrt{\tilde{\Gamma}_s}\,\frac{r}{r_2}\right) + c_2\, Y_0\left(\lambda\sqrt{\tilde{\Gamma}_s}\,\frac{r}{r_2}\right), \tag{18}$$

where c_1, c_2 are constants, and where J_0 and Y_0 denote the Bessel functions of the first and second kind, respectively (Abramowitz & Stegun 1972). The boundary conditions $\partial h/\partial r \to 0$ as $r \to 0$ and $h(r_2) = 0$ then require $c_2 = 0$, noting that $J_0'(x) = -J_1(x)$, $Y_0'(x) = -Y_1(x)$, and $\lambda_n = j_{0,n}\big/\sqrt{\tilde{\Gamma}_s}$ where λ_n is the nth zero ($n = 1, 2, \ldots$) of the Bessel function

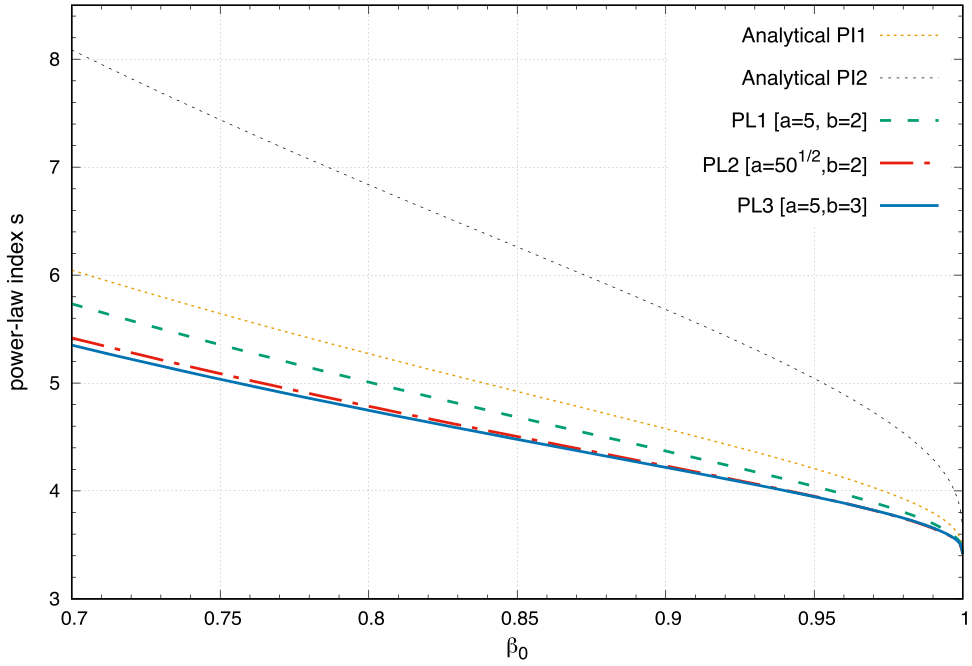

Figure 5. Evolution of the momentum power-law index s, where $f \propto p^{-s}$, as a function of the flow speed on the jet axis, $\beta_0 \equiv \beta(r=0)$, for spatially constant $\tau \propto p^{\alpha}$ with $\alpha = 1/3$. The dashed orange line (PI1) denotes the asymptotic spectral index as given in Equation (5) (Webb et al. 2018), and the dotted black line (PI2) denotes the asymptotic index as given in Equation (8) (Webb et al. 2019), both considering $\beta_2 = 0$. The three other lines denote the numerical solution for a power-law profile, Equation (11), with $a_p = 5$, $b = 2$ (dashed green line), $a_p = \sqrt{50}$, $b = 2$ (dashed–dotted red line), and $a_p = 5$, $b = 3$ (solid blue line).

J_0. For $n = 1$, a fundamental solution is thus fixed, implying $\lambda = \lambda_1 = -j_{0,1}/\sqrt{\tilde{\Gamma}_s}$, where $j_{0,1} = 2.4048$. With $g(p) \propto p^{-s}$ in the second differential Equation (17), one obtains $s_{1,2} = (3+\alpha)/2 \pm \sqrt{(3+\alpha)^2/4 + c^2\lambda^2/3}$, so that with the noted λ one obtains

$$s = \frac{3+\alpha}{2} + \sqrt{\frac{(3+\alpha)^2}{4} + \frac{c^2}{3}\frac{j_{0,1}^2}{\tilde{\Gamma}_s}} \tag{19}$$

for the power-law momentum index of the particle distribution above injection.

For the special case of a linearly decreasing profile, where Γ_s is a monotonically decreasing function, our previous choice of averaging (Rieger & Duffy 2019) turns out to work rather well. When the corresponding $\tilde{\Gamma}_s = (c^2/60)(\ln[(1+\beta_{02})/(1-\beta_{02})])^2$ is inserted in Equation (19) a reasonable approximation of the numerical solution is achieved (see Figure 6). The approximation in this case actually coincides with Equation (8) (see Webb et al. 2019). On the other hand, for a Gaussian and a power-law-type profile, for which Γ_s peaks on small scales (close to the axis), we find that a quasi-weighted average

$$\tilde{\Gamma}_s = \frac{c^2}{15}\frac{r_2^2\langle\gamma_b(r)^2(d\beta/dr)\rangle^2}{\langle\beta(r)\rangle} = \frac{c^2}{60\,\langle\beta(r)\rangle}\left(\ln\left[\frac{1+\beta_{02}}{1-\beta_{02}}\right]\right)^2 \tag{20}$$

with $\langle\beta(r)\rangle \equiv (\int_0^{r_2}\beta(r)dr)/(\int_0^{r_2}dr)$ yields a reasonable approximation when inserted in Equation (19); see Figure 6.

While approximate, using Equation (20) in Equation (19) thus provides a simple means of taking the shape of the velocity profile into account and improving the estimate for the momentum spectral index based on a leaky-box approach. This corresponds to replacing $\tau_{\rm esc}$ in the previous leaky-box equation (see Equations (1), (13), (15)) by $\tau_{\rm esc} \rightarrow \bar{\tau}\,\tau_{\rm esc}$, where $\bar{\tau} = 2/j_{01}^2$. The results above can in principle be used to facilitate a simple first-order comparison with observations.

4. Discussion and Conclusion

The results presented here confirm the intuitive notion that, in general, both the magnitude of the flow velocity and its explicit shear profile have an impact on the momentum spectrum generated in gradual shear particle acceleration. Considering spatially constant diffusion, we have explored several characteristic shear flow profiles, from a linearly decreasing to an exponentially decaying (Gaussian-type) velocity shear. When compared with each other, power-law-type velocity profiles provide the hardest (flattest) spectra.

In the absence of radiative losses, nonthermal shear particle acceleration results in power-law momentum spectra. At ultrarelativistic speeds ($\beta \rightarrow 1$), the momentum spectral index for the particle distribution $N(p) \propto p^2 f(p) \propto p^{2-s} \propto p^{-\tilde{q}}$ becomes independent of the shape of the velocity profile, $s \rightarrow (3+\alpha)$, corresponding to $\tilde{q} \rightarrow (1+\alpha)$, with α parameterizing the momentum dependence of the mean scattering time, $\tau = \lambda/c \propto p^{\alpha}$. On the other hand, for mildly relativistic speeds power-law momentum indices $s \simeq 4$, corresponding to $N(p) \propto p^{-2}$, are achievable, for example, for power-law-type flow profiles with Lorentz factors $\Gamma_0 \simeq 3$ ($\beta_0 \simeq 0.94$) and $\alpha = 1/3$.

We find that a simple leaky-box-type approach for relativistic shear acceleration captures the qualitative and quantitative (to within $\leqslant 10\%$) behavior of the momentum spectral index as a function of the on-axis speed β_0 for both

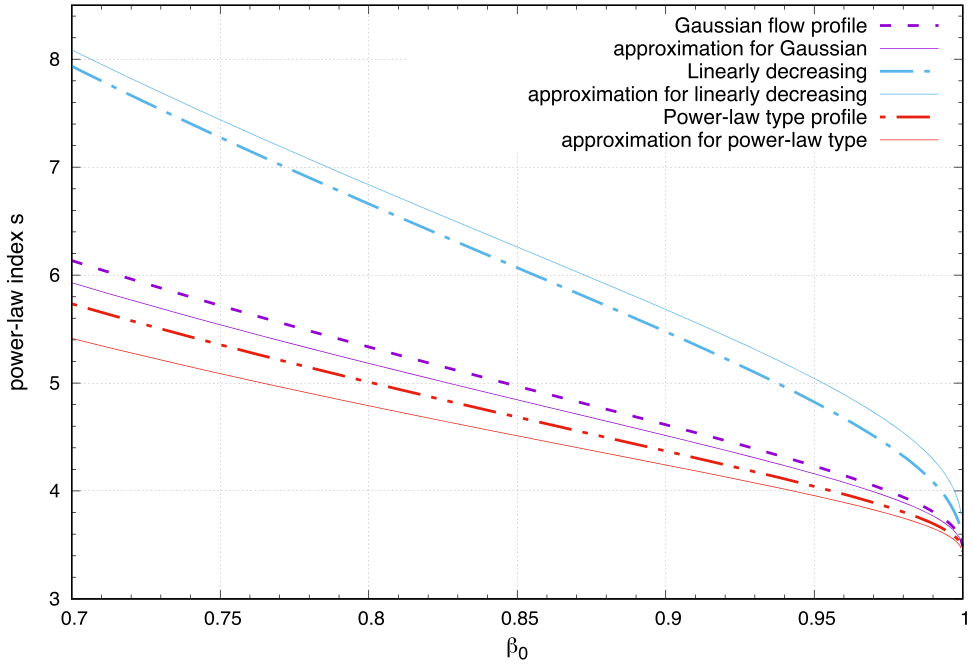

Figure 6. Evolution of the momentum power-law index s as a function of the flow speed on the jet axis, $\beta_0 \equiv \beta(r=0)$, for spatially constant $\tau \propto p^{\alpha}$ with $\alpha = 1/3$. The thick solid lines denote numerical solutions of the particle transport Equation (3) for a linearly decreasing, Gaussian, and power-law-type ($a_p = 5$, $b = 2$) profile, respectively, as in Figure 3. Thin solid lines represent approximations (see text and Equation (20) for details) based on a leaky-box approach. These approximations deviate from the exact results by less than ∼6%.

Gaussian and power-law-type velocity profiles with

$$s \simeq \frac{(3+\alpha)}{2} + \left[\frac{(3+\alpha)^2}{4} + 116\,\langle\beta\rangle\left(\ln\frac{1+\beta_{02}}{1-\beta_{02}}\right)^{-2}\right]^{1/2}, \tag{21}$$

where $\langle\beta\rangle < 1$ denotes a weighted, spatial average of the considered velocity profile, and $\beta_{02} = (\beta_0 - \beta_2)/(1+\beta_0\beta_2)$ is the relative velocity between the on-axis flow speed β_0 and flow speed β_2 at the outer jet (shear) boundary.

The treatment presented here does not include radiative losses (e.g., synchrotron). The latter could lead to a pileup in the particle distribution at the momentum scale where acceleration balances losses (e.g., Tavecchio 2021; Wang et al. 2021). Taking this constraint into account, our present findings are providing a useful guide to cosmic-ray or electron shear acceleration over the energy regime for which radiative losses might be neglected. The current study is limited to spatially constant diffusion in order to facilitate a comparison of different flow profiles. In principle, an extended analysis keeping $\tau(r, p)$ is desirable, but it is left to a future paper. However, the results presented here are of relevance for the interpretation of jetted, high-energy astrophysical sources such as AGNs, since nonthermal shear acceleration is a promising mechanism for the acceleration of charged particles to relativistic energies and thus possibly responsible for some of the high-energy radiation observed (Rieger 2019, for a review). For example, the recently detected, extended very high energy emission along the kiloparsec-scale jet of Centaurus A has been successfully modeled as inverse Compton emission by a relativistic electron distribution whose high-energy branch follows a power law with index $\tilde{q} = 3.85$ (H.E.S.S. Collaboration et al. 2020). This would be compatible with a Gaussian-type shear flow profile (provided $\beta_0 \sim 0.7$) or a power-law-type one (for intermediate $\beta_0 \sim 0.5$–0.6). If one takes bulk velocity estimates based on radio observations as reliable indicators of the maximum jet speed, which may not necessarily be the case, then this would suggest $\beta \sim 0.5$ (Hardcastle et al. 2003) and tend to favor power-law-type velocity profiles over Gaussian ones.

In conclusion, the results presented in this paper provide a foundation for relating the momentum power-law index inferred from spectral modeling to specific flow velocity profiles and establish a relationship between β_0 and a required power-law index s (or $\tilde{q}$), both of which might be observationally constrained for specific sources.

F.M.R. kindly acknowledges funding by the DFG under RI 1187/8-1.

Appendix

Figure 7 shows the evolution of the relativistic shear flow coefficient Γ_s for the velocity profiles studied in the current paper.

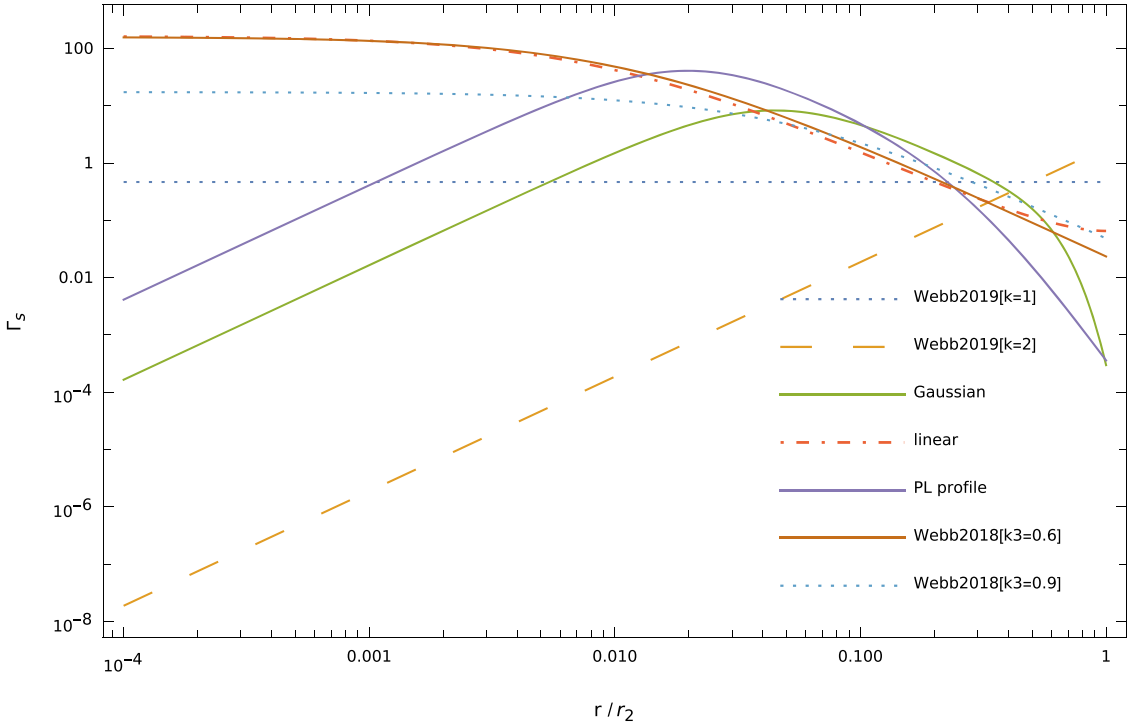

Figure 7. Illustration of the relativistic shear flow coefficient Γ_s, Equation (4), as a function of the normalized radial coordinate r/r_2 for flow profiles considered in this work and evaluated assuming $\beta_0 = 0.99$, i.e., Gaussian Equation (10) with $a_g = 5$; linearly decreasing Equation (9); power-law-type Equation (11) with $a_p = 5$, $b = 2$; concave-type profiles following Webb et al. (2019), Equation (7), for $k = 1$ and $k = 2$; and flow profiles following Webb et al. (2018), Equation (6), with $k_3 = 0.6$ and $k_3 = 0.9$, respectively. Gaussian and power-law-type profiles show a maximum (peak) on small spatial scales.

ORCID iDs

Frank M. Rieger https://orcid.org/0000-0003-1334-2993

References

Abramowitz, M., & Stegun, I. A. 1972, Handbook of Mathematical Functions (New York: Dover)
Berezhko, E. G. 1982, SvAL, 8, 403
Berezhko, E. G., & Krymskii, G. F. 1981, SvAL, 7, 352
Hardcastle, M. J., Worrall, D. M., Kraft, R. P., et al. 2003, ApJ, 593, 169
H.E.S.S. Collaboration, Abdalla, H., Adam, R., et al. 2020, Natur, 582, 356
Jokipii, J. R., & Morfill, G. E. 1990, ApJ, 356, 255
Lemoine, M. 2019, PhRvD, 99, 083006
Liu, R.-Y., Rieger, F. M., & Aharonian, F. A. 2017, ApJ, 842, 39
Merten, L., Boughelilba, M., Reimer, A., et al. 2021, APh, 128, 102564
Rieger, F. M. 2019, Galax, 7, 78
Rieger, F. M., & Duffy, P. 2006, ApJ, 652, 1044
Rieger, F. M., & Duffy, P. 2019, ApJL, 886, L26
Rieger, F. M., & Duffy, P. 2021, ApJL, 907, L2
Tavecchio, F. 2021, MNRAS, 501, 6199
Wang, J.-S., Reville, B., Liu, R.-Y., Rieger, F. M., & Aharonian, F. A. 2021, MNRAS, 505, 1334
Webb, G. M. 1989, ApJ, 340, 1112
Webb, G. M., Al-Nussirat, S., Mostafavi, P., et al. 2019, ApJ, 881, 123
Webb, G. M., Barghouty, A. F., Hu, Q., & le Roux, J. A. 2018, ApJ, 855, 31
Webb, G. M., Mostafavi, P., Al-Nussirat, S., et al. 2020, ApJ, 894, 95
Wolfram, R. I. 2022, Mathematica v13.0, https://www.wolfram.com/mathematica/